



Extreme events driving year-to-year differences in gross primary productivity across the US

Alexander J. Turner¹, Philipp Köhler², Troy S. Magney³, Christian Frankenberg^{2,4}, Inez Fung⁵, and Ronald C. Cohen^{5,6}

¹Department of Atmospheric Sciences, University of Washington, Seattle, WA 98195, USA

²Division of Geological and Planetary Sciences, California Institute of Technology, Pasadena, CA 91226, USA

³Department of Plant Sciences, University of California, Davis, Davis, CA 95616, USA

⁴Jet Propulsion Laboratory, California Institute of Technology, Pasadena, CA 91109, USA

⁵Department of Earth and Planetary Science, University of California, Berkeley, Berkeley, CA 94720, USA

⁶College of Chemistry, University of California, Berkeley, Berkeley, CA 94720, USA

Correspondence: Alexander J. Turner (turneraj@uw.edu)

Received: 23 February 2021 – Discussion started: 5 March 2021

Revised: 21 October 2021 – Accepted: 18 November 2021 – Published: 23 December 2021

Abstract. Solar-induced chlorophyll fluorescence (SIF) has previously been shown to strongly correlate with gross primary productivity (GPP); however this relationship has not yet been quantified for the recently launched TROPOspheric Monitoring Instrument (TROPOMI). Here we use a Gaussian mixture model to develop a parsimonious relationship between SIF from TROPOMI and GPP from flux towers across the conterminous United States (CONUS). The mixture model indicates the SIF–GPP relationship can be characterized by a linear model with two terms. We then estimate GPP across CONUS at 500 m spatial resolution over a 16 d moving window. We observe four extreme precipitation events that induce regional GPP anomalies: drought in western Texas, flooding in the midwestern US, drought in South Dakota, and drought in California. Taken together, these events account for 28 % of the year-to-year GPP differences across CONUS. Despite these large regional anomalies, we find that CONUS GPP varies by less than 4 % between 2018 and 2019.

1 Introduction

Terrestrial gross primary productivity (GPP) is the total amount of carbon dioxide (CO_2) assimilated by plants through photosynthesis and represents one of the main drivers of interannual variability in the global carbon cy-

cle (Le Quéré et al., 2018). As such, quantifying the spatiotemporal patterns of terrestrial GPP is critical to understanding how the carbon cycle will both respond to and influence climate. Work over the past decade has shown satellite measurements of solar-induced chlorophyll fluorescence (SIF) to correlate strongly with tower-based estimates of GPP (e.g., Frankenberg et al., 2011a; Yang et al., 2015; Sun et al., 2017; Turner et al., 2020; Wang et al., 2020) and are often used as a remote-sensing proxy for GPP.

This relationship between SIF and GPP is typically expressed through a pair of light use efficiency models (Monteith, 1972) that relate GPP and SIF to the absorbed photosynthetically active radiation (APAR):

$$\text{GPP} = \text{APAR} \times \Phi_{\text{CO}_2}, \quad (1)$$

$$\text{SIF} = \text{APAR} \times \beta \Phi_F, \quad (2)$$

where Φ_{CO_2} is the light use efficiency of CO_2 assimilation, Φ_F is the fluorescence yield, and β is the probability of fluoresced photons escaping the canopy. Solving for APAR and substituting, we can rewrite GPP as follows:

$$\text{GPP} = \frac{\Phi_{\text{CO}_2}}{\beta \Phi_F} \text{SIF}. \quad (3)$$

The derivation follows from Lee et al. (2013), Guanter et al. (2014), Sun et al. (2017), and others.

This seemingly straightforward relationship between SIF and GPP has been widely used to infer GPP from measurements of SIF (e.g., Frankenberg et al., 2011a; Parazoo et al.,

2014; Yang et al., 2015, 2017; Sun et al., 2017, 2018; Magney et al., 2019; Turner et al., 2020) with some work showing that SIF captures more variability in GPP than APAR alone (e.g., Yang et al., 2015, 2017; Magney et al., 2019). However, there is much complexity encapsulated in the first term of Eq. (3) ($\Phi_{CO_2}/\beta\Phi_F$). There is an ongoing debate about what *exactly* SIF is telling us about GPP (e.g., Joiner and Yoshida, 2020; Maguire et al., 2020; Dechant et al., 2020; He et al., 2020; Marrs et al., 2020) and the spatiotemporal scales at which SIF and GPP correlate well. A recent paper from Magney et al. (2020) presents a concise summary of the covariation between SIF and GPP at different spatiotemporal scales and how nonlinear relationships at the leaf scale often integrate to a linear response at the canopy scale. This is due, in large part, to the fact that most of our satellite measurements occur near the middle of the day when the Φ_{CO_2} - Φ_F response is more or less linear and the observed signal is integrated over many leaves.

Here we focus on the ecosystem-scale relationship between SIF and GPP, as that is the relevant observable scale from spaceborne instruments. We begin by characterizing the relationship between instantaneous SIF from the TROPOMI and half-hourly GPP from flux towers. Following this, we use this ecosystem-scale relationship to infer GPP at a spatial resolution of 500 m using TROPOMI SIF measurements and identify drivers of interannual variability in GPP. Previous work has identified effects and responses such as drought (e.g., Sun et al., 2015), flooding (Yin et al., 2020), and seasonal redistribution (Butterfield et al., 2020) as important factors controlling interannual variability in GPP.

2 Identifying distinct relationships between SIF and GPP

We build on our previous work (Turner et al., 2020) downscaling measurements of SIF to 500 m spatial resolution. Briefly, the TROPOspheric Monitoring Instrument (TROPOMI; Veefkind et al., 2012) is a nadir-viewing imaging spectrometer. TROPOMI has a 2600 km swath with a nadir spatial resolution of 5.6 km along track and 3.5 km across track. Köhler et al. (2018) presented the first retrievals of SIF from TROPOMI. As in Turner et al. (2020), we apply a post hoc bias correction to ensure positivity of monthly average values, as systematically negative SIF values are non-physical. We downscale individual TROPOMI scenes using the near-infrared reflectance of vegetation index (NIR_v) that was proposed by Badgley et al. (2017, 2019). We use the MCD43A4.006 (v06) MODIS NBAR (nadir BRDF-adjusted reflectance; bidirectional reflectance distribution function) reflectances (Schaaf et al., 2002) to compute NIR_v . Two notable differences from Turner et al. (2020) are the following: (1) the analysis is extended to cover all of CONUS, and (2) we now use a 16 d moving window, thus including

a full orbit cycle in each averaging window to minimize effects due to viewing-illumination geometry and noise. Supplement Fig. S3 shows the improvement when averaging to longer temporal windows with an r of 0.66, 0.74, 0.79, and 0.82 for instantaneous and 8, 16, and 32 d temporal windows, respectively.

The extension to CONUS facilitates comparison of TROPOMI SIF retrievals to flux tower data over a more representative set of ecosystems and robustly infers the SIF–GPP relationship. Specifically, there are 102 AmeriFlux sites (Baldocchi et al., 2001) within CONUS that reported data in 2018, 2019, or 2020, whereas (Turner et al., 2020) only included 11 sites and did not have data from forests. Figure 1 shows the location of these 102 AmeriFlux sites overlaid on the dominant land cover. These eddy covariance sites provide a direct measure of net ecosystem exchange (NEE; CO₂ fluxes) (Baldocchi et al., 1988). We compute GPP at each site using nighttime measurements of NEE as a proxy for ecosystem respiration (Reichstein et al., 2005) to partition the NEE into respiration and GPP. The AmeriFlux sites used here cover 10 ecosystems as defined by the International Geosphere-Biosphere Programme: evergreen needleleaf forest, deciduous broadleaf forest, mixed forest, grassland, cropland, wetland, woody savanna, savanna, open shrubland, and closed shrubland. These are the classifications reported with the AmeriFlux data as of July 2021 (<https://ameriflux.lbl.gov>, last access: 27 July 2021).

We characterize the relationship between TROPOMI SIF and AmeriFlux GPP by plotting downscaled SIF observations against daily GPP from the nearest AmeriFlux site (see Supplement Figs. S1–S3). The TROPOMI overpass time varies over the orbit cycle. Frankenberg et al. (2011b) presented a simple approach to compute a “daily corrected” SIF that accounts for variations in overpass time, length of day, and solar zenith angle:

$$\overline{SIF}(x, y, t) = SIF(x, y, \tau_s) \frac{\int_{\tau_0}^{\tau_f} \cos[SZA(x, y, \tau)] d\tau}{\cos[SZA(x, y, \tau_s)]}, \quad (4)$$

where $SIF(x, y, \tau_s)$ is the instantaneous SIF, SZA is the local solar zenith angle, τ_0 is sunrise, τ_f is sunset, and τ_s is the hour corresponding to the TROPOMI overpass time. We compare this daily corrected SIF against the daily GPP for each AmeriFlux site. Specifically, the seven steps we take here are as follows: (1) construct a time series of daily GPP from each AmeriFlux site; (2) apply the post hoc bias correction to the TROPOMI SIF data; (3) compute the daily correction for TROPOMI SIF data; (4) downscale TROPOMI scenes to 500 m spatial resolution using MODIS NIR_v ; (5) find all TROPOMI scenes that cover an AmeriFlux site; (6) construct a time series of SIF observations from the 500 m grid cell that contains the AmeriFlux site; and (7) regress coincident daily corrected TROPOMI SIF on daily AmeriFlux GPP with a bisquare regression. The bisquare regression was chosen due to robustness against outliers. Additionally, we

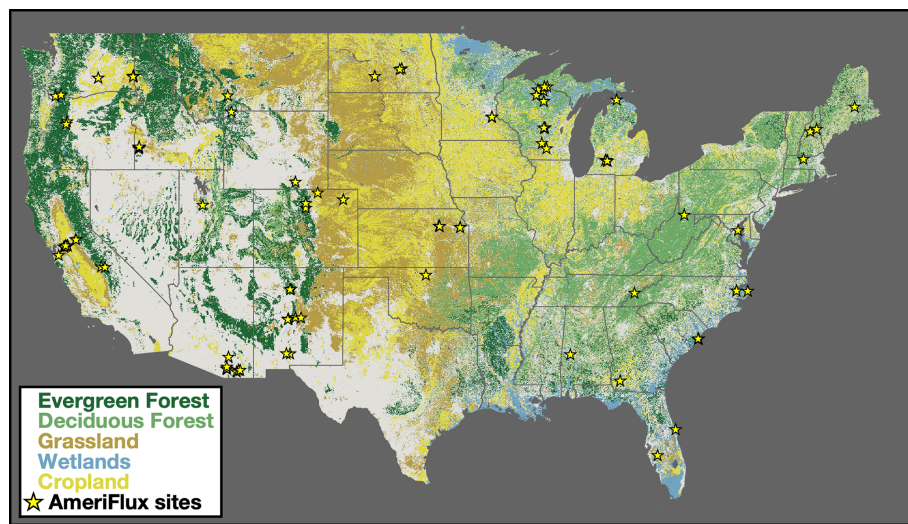


Figure 1. Dominant land cover over the conterminous United States (CONUS). Colors show the dominant land cover over CONUS. Classification is based on the 2019 USDA (United States Department of Agriculture) CropScape database (USDA, 2018). Forests are shown in green croplands in yellow, and wetlands are in blue. Location of 102 AmeriFlux sites used in this study are shown as yellow stars. See Table S1 for a list of all sites.

force the regression through the origin based on the physical constraint that GPP should be zero if SIF is zero. We observe a linear relationship between SIF and GPP when plotted against all ecosystems (Supplement Fig. S1) and when separated by ecosystem (Supplement Fig. S2). Notable exceptions are closed shrubland, open shrubland, and savanna ecosystems where SIF explains less than 10 % of the variability in GPP for AmeriFlux sites in those ecosystems due, in part, to a low signal-to-noise ratio. These ecosystems typically have a small SIF signal, and the bright surfaces often result in a higher retrieval uncertainty. This combination of a small signal and high retrieval uncertainty results in a low signal-to-noise ratio, complicating efforts to derive a robust relationship between SIF and GPP for these ecosystems.

Many of the ecosystems exhibit a similar linear relationship between SIF and GPP, which begs the following question: what ecosystems have a distinct SIF–GPP relationship? To address this, we bootstrap the bisquare regression for each ecosystem 2000 times. The slopes from this bootstrap can be seen in Fig. 2. The range of slopes vary from 13 to 18 ($\mu\text{mol m}^{-2} \text{s}^{-1}$) / ($\text{mW m}^{-2} \text{sr}^{-1} \text{s}^{-1}$) with grasslands at the low end and evergreen needleleaf forests at the high end. We then use a two-component Gaussian mixture model (see, for example, Bishop, 2007) to identify clusters of ecosystems with a similar SIF–GPP relationship. The implementation of our Gaussian mixture model is adapted from Turner and Jacob (2015). Parameters of the mixture model are obtained via an iterative expectation–maximization algorithm. A drawback of these mixture models is that they often find local minima. To address this, we repeat the fitting of the mixture model with multiple initializations and use simulated annealing to search for a global minimum. We tested a range

of mixture model sizes and found a mixture of two Gaussians to be the most robust. Adding additional terms in the model resulted in Gaussian functions that did not have the largest weighting factor for any ecosystem. This is because ecosystems like woody savanna and deciduous broadleaf have a large spread in their slope. As such, there is a lot of uncertainty, and the model does not find that they require a unique regression slope. The resulting mixture model is overlaid on the histogram in Fig. 2.

We observe a clustering of ecosystems with SIF–GPP relationships around $16.4 (\mu\text{mol m}^{-2} \text{s}^{-1}) / (\text{mW m}^{-2} \text{sr}^{-1} \text{s}^{-1})$. This grouping is the dominant weighting term for wetlands, evergreen needleleaf forests, deciduous broadleaf forests, mixed forests, cropland, and woody savanna. We refer to this cluster as the “dominant cluster” and assume that ecosystems not specifically mentioned elsewhere will have a response that is similar to this primary cluster. The other component of the mixture model corresponds to grasslands. Ecosystems not explicitly mentioned use the dominant cluster for scaling SIF to GPP. Table 1 lists the SIF–GPP relationships for these two clusters. The uncertainty is the variance for the Gaussian function for that particular cluster (see Bishop, 2007; Turner and Jacob, 2015, for more on Gaussian mixture models). Previous work has also found unique SIF–GPP relationships between C₃ and C₄ plants using measurements from a tower including a nonlinear response in C₃ plants (He et al., 2020); we examined this here using two AmeriFlux sites in corn fields and two in potato fields. We do observe potential differences in the SIF–GPP relationship between these C₃ and C₄ systems (see Supplement Fig. S5). The difference in the SIF–GPP relationship for C₃ and C₄ systems seen here is also similar to what was observed using NIR_V (Badgley et al., 2019).

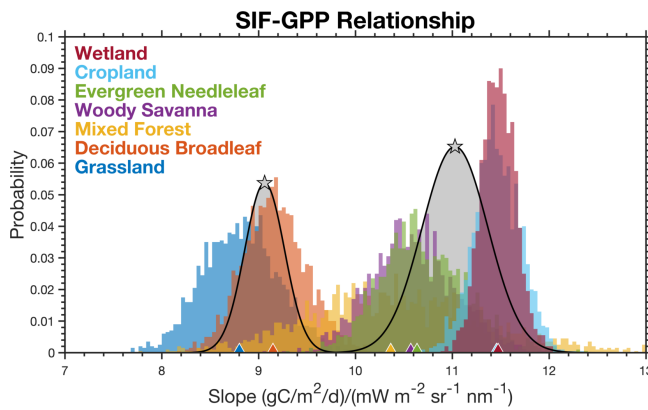


Figure 2. Identifying distinct SIF–GPP relationships across ecosystems. Histogram shows the distribution of slopes that map SIF to GPP using a bisquare regression and a 2000-member bootstrap. Colors denote the different ecosystems, and triangles at the bottom show the mean for that ecosystem. Gray distributions are from a two-member Gaussian mixture model, and the stars indicate the mean for that component.

Table 1. SIF–GPP relationships for different groupings.

Cluster	SIF–GPP relationship* (s_i)
Dominant cluster	9.1 ± 0.2
Grassland	11.0 ± 0.3

* All SIF–GPP relationships have units of $(\text{gC m}^{-2} \text{ d}^{-1}) / (\text{mW m}^{-2} \text{ sr}^{-1} \text{ nm}^{-1})$. Uncertainty is the diagonal of the covariance matrix for the mixture model.

These relationships can be used to reconstruct GPP from TROPOMI SIF as follows: $\text{GPP} = \text{SIF} \times (\sum_i f_i s_i)$, where s_i is the SIF–GPP relationship in Table 1 for the i th cluster and f_i is the fraction of a grid cell represented by that cluster.

TROPOMI is in low earth orbit and only observes a snapshot in time. The equatorial overpass time at nadir is 13:30 local time. We compute a daily corrected SIF that accounts for variations in overpass time, length of day, and solar zenith angle (Frankenberg et al., 2011b; Köhler et al., 2018):

$$\overline{\text{SIF}}(x, y, t) = \text{SIF}(x, y, \tau_s) \frac{\int_{\tau_0}^{\tau_f} \cos[\text{SZA}(x, y, \tau)] d\tau}{\cos[\text{SZA}(x, y, \tau_s)]}, \quad (5)$$

where $\text{SIF}(x, y, \tau_s)$ is the instantaneous SIF, SZA is the local solar zenith angle, τ_0 is sunrise, τ_f is sunset, and τ_s is the hour corresponding to the TROPOMI overpass time. More formally, we scale the instantaneous SIF by the ratio of the integral of the cosine of the solar zenith angle (SZA) over the day to $\cos(\text{SZA})$ from the TROPOMI overpass time. Putting everything together, we estimate daily GPP from TROPOMI SIF observations as follows:

$$\text{GPP}(x, y, t) = \overline{\text{SIF}}(x, y, t) \cdot \gamma \sum_i s_i f_i(x, y), \quad (6)$$

where $\text{SIF}(x, y, t)$ is the 500 m downsampled SIF using a 16 d moving window, γ is a unit conversion from μmol to gC , s_i

is the SIF–GPP relationship inferred from comparison with AmeriFlux GPP (see Table 1), $f_i(x, y)$ is the fraction of the grid cell represented by the i th cluster, SZA is the local solar zenith angle, τ_0 is sunrise, τ_f is sunset, and τ_s is the hour corresponding to the TROPOMI overpass time. We do not include information on cloud cover in our approach; this could potentially be included in the future to account for diurnal variations in PAR.

Our estimate of GPP is proportional to SIF and the regression coefficients: $\text{GPP} \propto \overline{\text{SIF}} \cdot \gamma \sum_i s_i f_i(x, y)$. As such, we propagate our uncertainties in quadrature:

$$\begin{aligned} \sigma_{\text{GPP}} &= \sqrt{\left(\frac{\partial \text{GPP}}{\partial \overline{\text{SIF}}} \sigma_{\overline{\text{SIF}}} \right)^2 + \sum_i \left(\frac{\partial \text{GPP}}{\partial s_i} \sigma_{s_i} \right)^2} \\ &= \sqrt{\left(\sigma_{\overline{\text{SIF}}} \gamma \sum_i s_i f_i(x, y) \right)^2} \\ &\quad + \sqrt{\left(\overline{\text{SIF}}(x, y, t) \cdot \sigma_{s_i} \gamma s_i f_i(x, y) \right)^2}, \end{aligned} \quad (7)$$

where $\sigma_{\overline{\text{SIF}}}$ is the uncertainty in the daily corrected SIF and σ_{s_i} is the uncertainty in the SIF–GPP relationship.

3 Drivers of interannual variations in US gross primary productivity

Figure 3 shows annual mean GPP across CONUS inferred from TROPOMI SIF measurements using Eq. (6). A number of prominent features are visible such as the Central Valley of California, the Snake River Valley in Idaho, and the Adirondack Mountains in upstate New York. California's Central Valley and Idaho's Snake River Valley are both major agricultural regions in the western US (e.g., the Central Valley of California accounts for more than 15 % of irrigated land in the US). The Adirondack Mountains are a roughly circular dome that rise above the surrounding lowlands, resulting in a shorter growing season and lower annual mean GPP. This shortened growing season can be seen in an animation of GPP over CONUS (Video Supplement).

We observe substantial GPP across the eastern US (delimited here by 98° W) with annual mean values generally in excess of $5 \text{ gC m}^{-2} \text{ d}^{-1}$. This region accounts for less than half of the land but more than 70 % of the annual GPP. This delineation in GPP roughly coincides with the location of drylands in CONUS that are more sensitive to changes in precipitation as inferred by measurements from the Global Precipitation Measurement (GPM) mission (specifically, we use the GPM_3IMERGDE.06 product); drylands are also projected to expand in future climate (Yao et al., 2020). Most of the large year-to-year differences occur in these western US drylands (see Fig. 3c), a notable exception being a negative GPP anomaly in 2019 relative to 2018 that extended across Illinois, Indiana, and Ohio. Here we highlight four precipitation-driven GPP anomalies, which taken together,

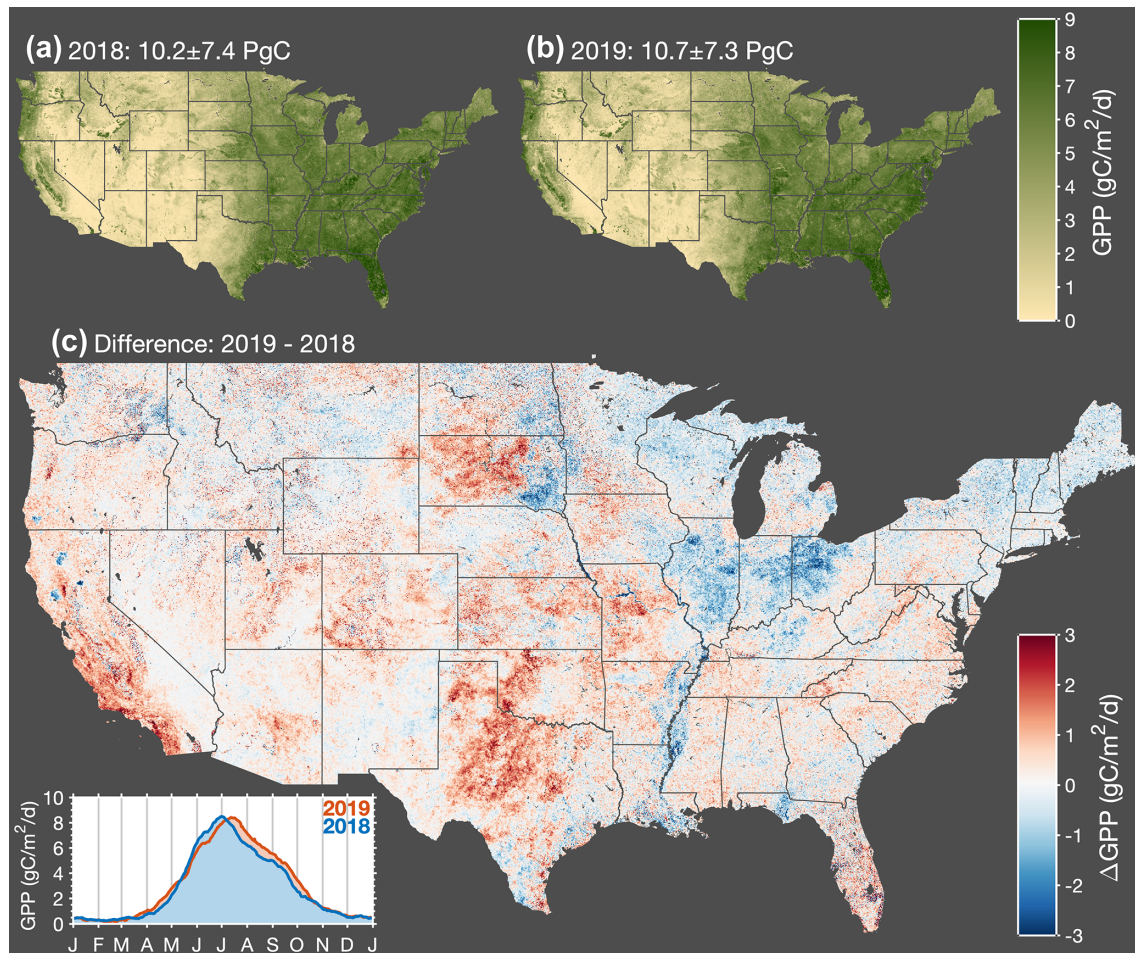


Figure 3. Interannual variations in gross primary productivity across CONUS. Map of annual mean GPP for 2018 (**a**) and 2019 (**b**). (**c**) Map of the difference in annual mean GPP between 2019 and 2018. Red indicates higher GPP in 2019, and blue indicates higher GPP in 2018. Inset in the bottom left corner shows a time series of the average GPP across CONUS for 2018 and 2019.

account for 28 % of the interannual GPP variability across the United States: (1) 2018 drought in western Texas, (2) 2019 midwestern crop flooding, (3) 2018 drought in South Dakota, and (4) 2018 drought in California. Figure 4 summarizes the interannual precipitation differences that we hypothesize are responsible for explaining these four GPP anomalies.

The largest positive GPP anomaly in 2019 relative to 2018 was observed across western Texas. This single event accounted for 11 % of the year-to-year difference in GPP across CONUS with an annual GPP of 0.65 ± 0.47 PgC in 2018 and 0.76 ± 0.45 PgC in 2019. From Fig. 4a, we observe 50 % higher GPP in spring 2019 compared to spring 2018. This increase in GPP was driven by a lack of precipitation in spring 2018. The cumulative precipitation from October 2017 through June 2018 was 50 % less than October 2018 through June 2019 (500 mm vs. 1000 mm). The other notable difference between GPP in 2018 and 2019 was a second peak during fall 2018 that was not present in 2019. This second peak coincided with a series of precipitation events

beginning in early September. This tight coupling between GPP and precipitation is expected for dryland systems such as western Texas (e.g., Smith et al., 2019). The seasonal GPP dynamics inferred from TROPOMI SIF are also present in the MODIS vegetation index NIR_v, albeit with slight differences in magnitude, implying convergent responses in SIF and NIR_v for this ecosystem.

The second largest anomaly is the reduction in 2019 GPP relative to 2018 across midwestern crop areas (specifically Illinois, Indiana, and Ohio) that accounted for 7 % of the year-to-year difference in CONUS GPP. The 2018 annual GPP was 0.70 ± 0.12 and 0.63 ± 0.14 PgC in 2019. We observe a decrease in the maximum GPP between 2019 and 2018 as well as a 2-week delay in the timing of the maximum. This anomaly was highlighted in recent work from Yin et al. (2020), who attribute the anomaly to flooding in the midwestern US. The flooding delayed the planting of crops by 2 weeks and resulted in decreased carbon uptake across the midwestern crop areas and Mississippi Alluvial Valley,

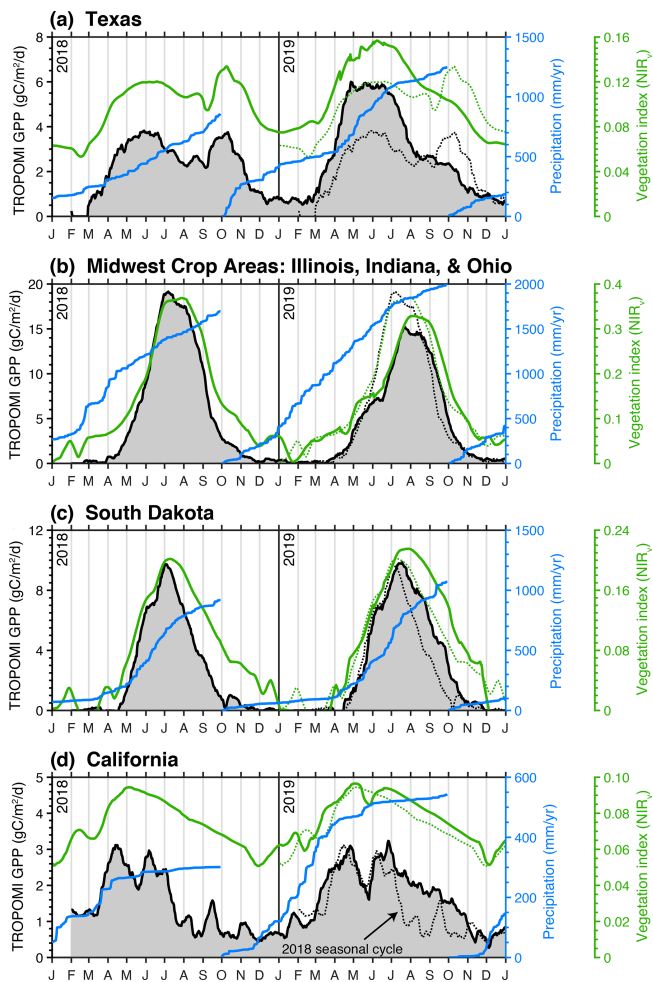


Figure 4. Major drivers of interannual variability in CONUS GPP. Black line shows the TROPOMI-derived GPP over Texas (**a**), the midwestern crop region (**b**), South Dakota (**c**), and California (**d**). Blue line shows the cumulative precipitation over the water year as measured by the GPM satellite. Green line is NIR_v from MODIS. Black and green dotted lines are 2018 GPP and NIR_v superimposed on the 2019 time series.

where we also observe a negative anomaly in Fig. 3c. Yin et al. (2020) provide a detailed discussion of these floods and their impacts on crop productivity.

South Dakota exhibits a dipole with positive anomalies in 2019 in the west and negative anomalies in the east, again relative to 2018. The 2018 annual GPP was 0.20 ± 0.09 and $0.63 \pm 0.08 \text{ PgC}$ in 2019. The negative anomalies in the east are driven by the flooding events discussed above and in Yin et al. (2020). However, the positive anomaly in the western portion of the state is the dominant term. This positive anomaly is driven by a series of summer precipitation events that served to extend the growing season across the western plains. From Fig. 4c, we can see three precipitation events throughout the mid-to-late summer that coincide with pauses in senescence: mid-July, early August, and mid-September.

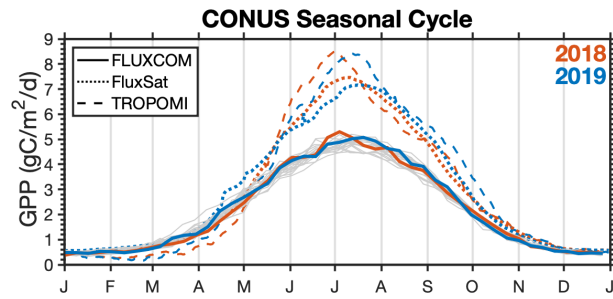


Figure 5. Comparison of the seasonal cycle inferred from TROPOMI SIF to FluxCom and FluxSat. Red lines indicate the 2018 seasonal cycle, and blue lines indicate the 2019 seasonal cycle for TROPOMI (dashed lines), FluxSat (dotted lines), and FluxCom (solid lines). Thin gray lines are years 2001–2017 for FluxCom.

As with Texas, this highlights the tight coupling between GPP and precipitation for dryland systems. In total, these precipitation events served to increase statewide GPP in 2019 relative to 2018.

The final notable anomaly is California's positive GPP anomaly in 2019. The 2018 annual GPP was 0.27 ± 0.24 and $0.33 \pm 0.26 \text{ PgC}$ in 2019. The year 2018 had a mild drought in California with $\sim 80\%$ of the state being classified as abnormally dry; 2019 had 50% more precipitation during the water year than 2018 (Fig. 4c). Two consequences of this drought in 2018 were a delayed onset of photosynthesis and a mid-summer senescence. The onset of photosynthesis in 2018 coincided with a series of atmospheric rivers that delivered about a third of the total precipitation that year, indicating a water limitation up to that point. In contrast, 2019 had ample precipitation through the winter, and we observe both an earlier onset of photosynthesis and an extension of the growing season into the fall. Evergreen forests are the main contributor to the SIF signal during the summer and fall (Turner et al., 2020) and, as such, will be more sensitive to the accumulated precipitation. The spatial pattern of the differences in August–November GPP (Fig. S4) strongly correlate with evergreen forests.

In contrast to the anomalies presented earlier, the SIF-derived GPP and MODIS-based vegetation index (NIR_v) show divergent seasonal dynamics for California. NIR_v shows small differences between 2018 and 2019 with a strong similarity to the 2019 SIF-derived GPP. The seasonality of NIR_v is similar to that of the leaf area index (LAI) derived from MODIS (see Supplement Fig. S6), implying a biophysical signal. Vegetation indices derived from the red and NIR part of the spectrum estimate *photosynthetic capacity* provided optimal soil moisture, temperature, and PAR are known (Sellers, 1985). As such, this suggests that we observed a downregulation of photosynthesis from evergreen forests in response to a water limitation during fall 2018, whereas these forests were close to photosynthetic capacity in fall 2019 resulting in a similar seasonality to 2018 and

2019 NIR_v . Sims et al. (2014) also report a low sensitivity of MODIS vegetation indices to drought stress in forests.

We additionally compare our GPP estimated from TROPOMI SIF to previous work developing gridded GPP products using machine learning. Specifically, the FluxCom initiative (<http://www.fluxcom.org/>, last access: 27 July 2021 Jung et al., 2020) and FluxSat (Joiner and Yoshida, 2020) independently trained machine-learning models to predict gridded GPP from eddy covariance sites using remote-sensing data (including MODIS). Figure 5 shows the CONUS seasonal cycle from FluxCom, FluxSat, and TROPOMI. The seasonal cycles of GPP inferred from TROPOMI and FluxSat are generally in agreement with a similar magnitude, while FluxCom predicts 35 % less GPP. Additionally, the interannual variability in GPP over CONUS inferred from TROPOMI SIF is larger than what is predicted by either FluxCom or FluxSat, both of which show little interannual variability. The low interannual variability is particularly evident in FluxCom, where we can see a small spread in the variability from 2001 to 2017 (gray lines).

4 Conclusions

We have developed a parsimonious relationship between measurements of SIF from TROPOMI and GPP inferred from flux towers. This relationship allows for the estimation of GPP directly from TROPOMI SIF measurements. We combine this SIF–GPP relationship with work downscaling TROPOMI data to 500 m spatial resolution to construct estimates of GPP across the conterminous United States in 2018 and 2019. We observe large regional anomalies that are driven by extreme precipitation events. Namely, western Texas, South Dakota, and California experienced droughts in 2018, while midwestern US crop areas (Illinois, Indiana, and Ohio) experienced flooding in 2019. Taken together, these four events account for 28 % of the year-to-year variability in GPP across the conterminous United States. Despite these large regional anomalies, our estimate of US GPP varies by less than 4 % between 2018 and 2019.

The impact of the western Texas drought, South Dakota drought, and midwestern flooding are observed in other remote-sensing measures of photosynthetic capacity such as NIR_v , while the California drought shows a divergent result using SIF; the divergent responses are driven by specific ecosystems such as evergreen forests. Our work suggests that SIF provides a measure of *photosynthetic activity* as opposed to photosynthetic capacity and converges with other remote-sensing measures under nonstressed conditions. Future work investigating the response to extreme events in evergreen systems may provide additional insight into these divergent responses in remote-sensing measurements related to photosynthesis.

Data availability. Daily gridded 500 m TROPOMI SIF and GPP data from 1 February 2018 through 15 June 2020 are temporarily available on Google Drive at <https://bit.ly/2GHEOOq> and has been uploaded to the ORNL DAAC at <https://doi.org/10.3334/ORNLDaac/1875> (Turner et al., 2021b).

Video supplement. Animation showing multiple years of GPP inferred from TROPOMI SIF. The Video Supplement can be found in the Supplement file below.

Supplement. The supplement related to this article is available online at: <https://doi.org/10.5194/bg-18-6579-2021-supplement>.

Author contributions. AJT wrote the text with feedback from all authors. PK and CF performed the TROPOMI SIF retrievals. AJT downscaled the SIF data, conducted the AmeriFlux analysis, and drafted the figures. All authors contributed to the discussion and analysis.

Competing interests. The contact author has declared that neither they nor their co-authors have any competing interests.

Disclaimer. Publisher's note: Copernicus Publications remains neutral with regard to jurisdictional claims in published maps and institutional affiliations.

Acknowledgements. We are grateful to the team that has realized the TROPOMI instrument, consisting of the partnership between Airbus Defence and Space, KNMI, SRON, and TNO, commissioned by NSO and ESA. We acknowledge the following AmeriFlux sites for their data records: US-ALQ, US-ARM, US-Bi1, US-Bi2, US-CF1, US-CF2, US-CF3, US-CF4, US-CS1, US-CS2, US-CS3, US-EDN, US-GLE, US-Hn2, US-Hn3, US-Ho1, US-JRn, US-Jo2, US-KS3, US-Los, US-Me2, US-Me6, US-Men, US-Mpj, US-MtB, US-Myb, US-NC2, US-NC3, US-NC4, US-Rls, US-Rms, US-Ro4, US-Ro5, US-Ro6, US-Rwf, US-Rws, US-SRG, US-SRM, US-Seg, US-Ses, US-Sne, US-Snf, US-Syy, US-Ton, US-Tw1, US-Tw4, US-Tw5, US-UMd, US-Var, US-Vcm, US-Vcp, US-WCr, US-Whs, US-Wjs, US-Wkg, US-xAB, US-xBR, US-xCP, US-xDC, US-xDL, US-xHA, US-xJE, US-xJR, US-xKA, US-xKZ, US-xNG, US-xNQ, US-xRM, US-xSE, US-xSL, US-xSP, US-xSR, US-xST, US-xTE, US-xUK, US-xUN, US-xWD, US-xWR, and US-xYE. In addition, funding for AmeriFlux data resources was provided by the U.S. Department of Energy's Office of Science.

Financial support. Alexander J. Turner was supported by the NASA Carbon Cycle Science program (grant no. 80HQTR21T0101), the NASA Early Career Faculty program (grant 80NSSC21K1808), and as a Miller Fellow with the Miller Institute for Basic Research in Science at the University of California (UC), Berkeley. This research was funded by grants

from the Koret Foundation and NASA (no. 80NSSC19K0945) for support of the computational resources. Part of this research was funded by the NASA Carbon Cycle Science program (grant no. NNX17AE14G). TROPOMI SIF data generation by Philipp Köhler and Christian Frankenberg is funded by the Earth Science U.S. Participating Investigator program (grant no. NNX15AH95G). Troy S. Magney was supported through the Macrosystems Biology and NEON-Enabled Science program (grant no. DEB-579 1926090). This research used the Savio computational cluster resource provided by the Berkeley Research Computing program at the University of California, Berkeley (supported by the UC Berkeley Chancellor, Vice Chancellor for Research, and Chief Information Officer).

Review statement. This paper was edited by Paul Stoy and reviewed by two anonymous referees.

References

- Badgley, G., Field, C. B., and Berry, J. A.: Canopy near-infrared reflectance and terrestrial photosynthesis, *Sci. Adv.*, 3, e1602244, <https://doi.org/10.1126/sciadv.1602244>, 2017.
- Badgley, G., Anderegg, L. D. L., Berry, J. A., and Field, C. B.: Terrestrial Gross Primary Production: Using NIR_{V} to Scale from Site to Globe, *Glob. Change Biol.*, 25, 3731–3740, <https://doi.org/10.1111/gcb.14729>, 2019.
- Baldocchi, D., Falge, E., Gu, L., Olson, R., Hollinger, D., Running, S., Anthoni, P., Bernhofer, C., Davis, K., Evans, R., Fuentes, J., Goldstein, A., Katul, G., Law, B., Lee, X., Malhi, Y., Meyers, T., Munger, W., Oechel, W., Paw, K. T., Pilegaard, K., Schmid, H. P., Valentini, R., Verma, S., Vesala, T., Wilson, K., and Wofsy, S.: FLUXNET: A New Tool to Study the Temporal and Spatial Variability of Ecosystem-Scale Carbon Dioxide, Water Vapor, and Energy Flux Densities, *Bull. Am. Meteorol. Soc.*, 82, 2415–2434, [https://doi.org/10.1175/1520-0477\(2001\)082<2415:fants>2.3.co;2](https://doi.org/10.1175/1520-0477(2001)082<2415:fants>2.3.co;2), 2001.
- Baldocchi, D. D., Hicks, B. B., and Meyers, T. P.: Measuring Biosphere-Atmosphere Exchanges of Biologically Related Gases with Micrometeorological Methods, *Ecology*, 69, 1331–1340, <https://doi.org/10.2307/1941631>, 1988.
- Bishop, C. M.: Pattern Recognition and Machine Learning, Springer, 1st Edn., New York, NY, 2007.
- Butterfield, Z., Buermann, W., and Keppel-Aleks, G.: Satellite observations reveal seasonal redistribution of northern ecosystem productivity in response to interannual climate variability, *Remote Sens. Environ.*, 242, 111755, <https://doi.org/10.1016/j.rse.2020.111755>, 2020.
- Dechant, B., Ryu, Y., Badgley, G., Zeng, Y., Berry, J. A., Zhang, Y., Goulas, Y., Li, Z., Zhang, Q., Kang, M., Li, J., and Moya, I.: Canopy structure explains the relationship between photosynthesis and sun-induced chlorophyll fluorescence in crops, *Remote Sens. Environ.*, 241, 111733, <https://doi.org/10.1016/j.rse.2020.111733>, 2020.
- Frankenberg, C., Butz, A., and Toon, G. C.: Disentangling chlorophyll fluorescence from atmospheric scattering effects in O_2A -band spectra of reflected sun-light, *Geophys. Res. Lett.*, 38, L03801, <https://doi.org/10.1029/2010gl045896>, 2011a.
- Frankenberg, C., Fisher, J. B., Worden, J., Badgley, G., Saatchi, S. S., Lee, J.-E., Toon, G. C., Butz, A., Jung, M., Kuze, A., and Yokota, T.: New global observations of the terrestrial carbon cycle from GOSAT: Patterns of plant fluorescence with gross primary productivity, *Geophys. Res. Lett.*, 38, L17706, <https://doi.org/10.1029/2011gl048738>, 2011b.
- Guanter, L., Zhang, Y., Jung, M., Joiner, J., Voigt, M., Berry, J. A., Frankenberg, C., Huete, A. R., Zarco-Tejada, P., Lee, J. E., Moran, M. S., Ponce-Campos, G., Beer, C., Camps-Valls, G., Buchmann, N., Gianelle, D., Klumpp, K., Cescatti, A., Baker, J. M., and Griffis, T. J.: Global and time-resolved monitoring of crop photosynthesis with chlorophyll fluorescence, *P. Natl. Acad. Sci. USA*, 111, E1327–E1333, <https://doi.org/10.1073/pnas.1320008111>, 2014.
- He, L., Magney, T., Dutta, D., Yin, Y., Köhler, P., Grossmann, K., Stutz, J., Dold, C., Hatfield, J., Guan, K., Peng, B., and Frankenberg, C.: From the Ground to Space: Using Solar-Induced Chlorophyll Fluorescence to Estimate Crop Productivity, *Geophys. Res. Lett.*, 47, e2020GL087474, <https://doi.org/10.1029/2020gl087474>, 2020.
- Joiner, J. and Yoshida, Y.: Satellite-based reflectances capture large fraction of variability in global gross primary production (GPP) at weekly time scales, *Agr. Forest Meteorol.*, 291, 108092, <https://doi.org/10.1016/j.agrformet.2020.108092>, 2020.
- Jung, M., Schwalm, C., Migliavacca, M., Walther, S., Camps-Valls, G., Koitala, S., Anthoni, P., Besnard, S., Bodesheim, P., Carvalhais, N., Chevallier, F., Gans, F., Goll, D. S., Haverd, V., Köhler, P., Ichii, K., Jain, A. K., Liu, J., Lombardozzi, D., Nabel, J. E. M. S., Nelson, J. A., O'Sullivan, M., Pallandt, M., Papale, D., Peters, W., Pongratz, J., Rödenbeck, C., Sitch, S., Tramontana, G., Walker, A., Weber, U., and Reichstein, M.: Scaling carbon fluxes from eddy covariance sites to globe: synthesis and evaluation of the FLUXCOM approach, *Biogeosciences*, 17, 1343–1365, <https://doi.org/10.5194/bg-17-1343-2020>, 2020.
- Köhler, P., Frankenberg, C., Magney, T. S., Guanter, L., Joiner, J., and Landgraf, J.: Global Retrievals of Solar-Induced Chlorophyll Fluorescence With TROPOMI: First Results and Inter-sensor Comparison to OCO-2, *Geophys. Res. Lett.*, 45, 10456–10463, <https://doi.org/10.1029/2018gl079031>, 2018.
- Le Quéré, C., Andrew, R. M., Friedlingstein, P., Sitch, S., Hauck, J., Pongratz, J., Pickers, P. A., Korsbakken, J. I., Peters, G. P., Canadell, J. G., Arneth, A., Arora, V. K., Barbero, L., Bastos, A., Bopp, L., Chevallier, F., Chini, L. P., Ciais, P., Doney, S. C., Grätz, T., Goll, D. S., Harris, I., Haverd, V., Hoffman, F. M., Hoppema, M., Houghton, R. A., Hurtt, G., Ilyina, T., Jain, A. K., Johannessen, T., Jones, C. D., Kato, E., Keeling, R. F., Goldewijk, K. K., Landschützer, P., Lefévre, N., Lienert, S., Liu, Z., Lombardozzi, D., Metzl, N., Munro, D. R., Nabel, J. E. M. S., Nakao, S.-i., Neill, C., Olsen, A., Ono, T., Patra, P., Peregon, A., Peters, W., Peylin, P., Pfeil, B., Pierrot, D., Poulter, B., Redder, G., Resplandy, L., Robertson, E., Rocher, M., Rödenbeck, C., Schuster, U., Schwinger, J., Séférian, R., Skjelvan, I., Steinhoff, T., Sutton, A., Tans, P. P., Tian, H., Tilbrook, B., Tubiello, F. N., van der Laan-Luijkx, I. T., van der Werf, G. R., Viovy, N., Walker, A. P., Wiltshire, A. J., Wright, R., Zaehle, S., and Zheng, B.: Global Carbon Budget 2018, *Earth Syst. Sci. Data*, 10, 2141–2194, <https://doi.org/10.5194/essd-10-2141-2018>, 2018.
- Lee, J. E., Frankenberg, C., van der Tol, C., Berry, J. A., Guanter, L., Boyce, C. K., Fisher, J. B., Morrow, E., Worden,

- J. R., Asefi, S., Badgley, G., and Saatchi, S.: Forest productivity and water stress in Amazonia: observations from GOSAT chlorophyll fluorescence, *Proc. Biol. Sci.*, 280, 20130171, <https://doi.org/10.1098/rspb.2013.0171>, 2013.
- Magney, T. S., Bowling, D. R., Logan, B. A., Grossmann, K., Stutz, J., Blanken, P. D., Burns, S. P., Cheng, R., Garcia, M. A., Köhler, P., Lopez, S., Parazoo, N. C., Racza, B., Schimel, D., and Frankenberg, C.: Mechanistic evidence for tracking the seasonality of photosynthesis with solar-induced fluorescence, *P. Natl. Acad. Sci. USA*, 116, 11640–11645, <https://doi.org/10.1073/pnas.1900278116>, 2019.
- Magney, T. S., Barnes, M. L., and Yang, X.: On the Co-variation of Chlorophyll Fluorescence and Photosynthesis Across Scales, *Geophys. Res. Lett.*, 47, e2020GL091098, <https://doi.org/10.1029/2020gl091098>, 2020.
- Maguire, A. J., Eitel, J. U. H., Griffin, K. L., Magney, T. S., Long, R. A., Vierling, L. A., Schmiege, S. C., Jennewein, J. S., Weygant, W. A., Boelman, N. T., and Bruner, S. G.: On the Functional Relationship Between Fluorescence and Photochemical Yields in Complex Evergreen Needleleaf Canopies, *Geophys. Res. Lett.*, 47, e2020GL087858, <https://doi.org/10.1029/2020gl087858>, 2020.
- Marrs, J. K., Reblin, J. S., Logan, B. A., Allen, D. W., Reinmann, A. B., Bombard, D. M., Tabachnik, D., and Hutyra, L. R.: Solar-Induced Fluorescence Does Not Track Photosynthetic Carbon Assimilation Following Induced Stomatal Closure, *Geophys. Res. Lett.*, 47, e2020GL087956, <https://doi.org/10.1029/2020gl087956>, 2020.
- Monteith, J. L.: Solar Radiation and Productivity in Tropical Ecosystems, *J. Appl. Ecol.*, 9, 747–766, 1972.
- Parazoo, N. C., Bowman, K., Fisher, J. B., Frankenberg, C., Jones, D. B., Cescatti, A., Perez-Priego, O., Wohlfahrt, G., and Montagnani, L.: Terrestrial gross primary production inferred from satellite fluorescence and vegetation models, *Glob. Change Biol.*, 20, 3103–21, <https://doi.org/10.1111/gcb.12652>, 2014.
- Reichstein, M., Falge, E., Baldocchi, D., Papale, D., Aubinet, M., Berbigier, P., Bernhofer, C., Buchmann, N., Gilmanov, T., Granier, A., Grunwald, T., Havrankova, K., Ilvesniemi, H., Janous, D., Knohl, A., Laurila, T., Lohila, A., Loustau, D., Matteucci, G., Meyers, T., Miglietta, F., Ourcival, J.-M., Pumpanen, J., Rambal, S., Rotenberg, E., Sanz, M., Tenhunen, J., Seufert, G., Vaccari, F., Vesala, T., Yakir, D., and Valentini, R.: On the separation of net ecosystem exchange into assimilation and ecosystem respiration: review and improved algorithm, *Glob. Change Biol.*, 11, 1424–1439, <https://doi.org/10.1111/j.1365-2486.2005.001002.x>, 2005.
- Schaaf, C. B., Gao, F., Strahler, A. H., Lucht, W., Li, X., Tsang, T., Strugnell, N. C., Zhang, X., Jin, Y., Muller, J.-P., Lewis, P., Barnsley, M., Hobson, P., Disney, M., Roberts, G., Dunderdale, M., Doll, C., d'Entremont, R. P., Hu, B., Liang, S., Privette, J. L., and Roy, D.: First operational BRDF, albedo nadir reflectance products from MODIS, *Remote Sens. Environ.*, 83, 135–148, [https://doi.org/10.1016/s0034-4257\(02\)00091-3](https://doi.org/10.1016/s0034-4257(02)00091-3), 2002.
- Sellers, P. J.: Canopy reflectance, photosynthesis and transpiration, *Int. J. Remote Sens.*, 6, 1335–1372, <https://doi.org/10.1080/01431168508948283>, 1985.
- Sims, D. A., Brzostek, E. R., Rahman, A. F., Dragoni, D., and Phillips, R. P.: An improved approach for remotely sensing wa- ter stress impacts on forest C uptake, *Glob. Change Biol.*, 20, 2856–2866, <https://doi.org/10.1111/gcb.12537>, 2014.
- Smith, W. K., Dannenberg, M. P., Yan, D., Herrmann, S., Barnes, M. L., Barron-Gafford, G. A., Biederman, J. A., Ferrenberg, S., Fox, A. M., Hudson, A., Knowles, J. F., MacBean, N., Moore, D. J. P., Nagler, P. L., Reed, S. C., Rutherford, W. A., Scott, R. L., Wang, X., and Yang, J.: Remote sensing of dryland ecosystem structure and function: Progress, challenges, and opportunities, *Remote Sens. Environ.*, 233, 111401, <https://doi.org/10.1016/j.rse.2019.111401>, 2019.
- Sun, Y., Fu, R., Dickinson, R., Joiner, J., Frankenberg, C., Gu, L., Xia, Y., and Fernando, N.: Drought onset mechanisms revealed by satellite solar-induced chlorophyll fluorescence: Insights from two contrasting extreme events, *J. Geophys. Res.-Biogeo.*, 120, 2427–2440, <https://doi.org/10.1002/2015jg003150>, 2015.
- Sun, Y., Frankenberg, C., Wood, J. D., Schimel, D. S., Jung, M., Guanter, L., Drewry, D. T., Verma, M., Porcar-Castell, A., Griffis, T. J., Gu, L., Magney, T. S., Kohler, P., Evans, B., and Yuen, K.: OCO-2 advances photosynthesis observation from space via solar-induced chlorophyll fluorescence, *Science*, 358, eaam5747, <https://doi.org/10.1126/science.aam5747>, 2017.
- Sun, Y., Frankenberg, C., Jung, M., Joiner, J., Guanter, L., Köhler, P., and Magney, T.: Overview of Solar-Induced chlorophyll Fluorescence (SIF) from the Orbiting Carbon Observatory-2: Retrieval, cross-mission comparison, and global monitoring for GPP, *Remote Sens. Environ.*, 209, 808–823, <https://doi.org/10.1016/j.rse.2018.02.016>, 2018.
- Turner, A. J. and Jacob, D. J.: Balancing aggregation and smoothing errors in inverse models, *Atmos. Chem. Phys.*, 15, 7039–7048, <https://doi.org/10.5194/acp-15-7039-2015>, 2015.
- Turner, A. J., Köhler, P., Magney, T. S., Frankenberg, C., Fung, I., and Cohen, R. C.: A double peak in the seasonality of California's photosynthesis as observed from space, *Biogeosciences*, 17, 405–422, <https://doi.org/10.5194/bg-17-405-2020>, 2020.
- Turner, A. J., Koehler, P., Magney, T., Frankenberg, C., Fung, I., and Cohen, R. C.: CMS: Daily Gross Primary Productivity over CONUS from TROPOMI SIF, 2018–2020, ORNL DAAC [data set], Oak Ridge, Tennessee, USA, <https://doi.org/10.3334/ORNLDaac/1875>, 2021.
- USDA: National Agricultural Statistics Service Cropland Data Layer: Published crop-specific data layer, available at: <https://nassgeodata.gmu.edu/CropScape/> (last access: 27 July 2021), 2018.
- Veefkind, J. P., Aben, I., McMullan, K., Förster, H., de Vries, J., Otter, G., Claas, J., Eskes, H. J., de Haan, J. F., Kleipool, Q., van Weele, M., Hasekamp, O., Hoogeveen, R., Landgraf, J., Snel, R., Tol, P., Ingmann, P., Voors, R., Kruizinga, B., Vink, R., Visser, H., and Levelt, P. F.: TROPOMI on the ESA Sentinel-5 Precursor: A GMES mission for global observations of the atmospheric composition for climate, air quality and ozone layer applications, *Proc SPIE*, 120, 70–83, <https://doi.org/10.1016/j.rse.2011.09.027>, 2012.
- Wang, X., Dannenberg, M. P., Yan, D., Jones, M. O., Kimball, J. S., Moore, D. J. P., Leeuwen, W. J. D., Didan, K., and Smith, W. K.: Globally Consistent Patterns of Asynchrony in Vegetation Phenology Derived From Optical, Microwave, and Fluorescence Satellite Data, *J. Geophys. Res.-Biogeo.*, 125, e2020JG005732, <https://doi.org/10.1029/2020jg005732>, 2020.

- Yang, H., Yang, X., Zhang, Y., Heskel, M. A., Lu, X., Munger, J. W., Sun, S., and Tang, J.: Chlorophyll fluorescence tracks seasonal variations of photosynthesis from leaf to canopy in a temperate forest, *Glob. Change Biol.*, 23, 2874–2886, <https://doi.org/10.1111/gcb.13590>, 2017.
- Yang, X., Tang, J., Mustard, J. F., Lee, J.-E., Rossini, M., Joiner, J., Munger, J. W., Kornfeld, A., and Richardson, A. D.: Solar-induced chlorophyll fluorescence that correlates with canopy photosynthesis on diurnal and seasonal scales in a temperate deciduous forest, *Geophys. Res. Lett.*, 42, 2977–2987, <https://doi.org/10.1002/2015gl063201>, 2015.
- Yao, J., Liu, H., Huang, J., Gao, Z., Wang, G., Li, D., Yu, H., and Chen, X.: Accelerated dryland expansion regulates future variability in dryland gross primary production, *Nat. Commun.*, 11, 1665, <https://doi.org/10.1038/s41467-020-15515-2>, 2020.
- Yin, Y., Byrne, B., Liu, J., Wennberg, P. O., Davis, K. J., Magney, T., Köhler, P., He, L., Jeyaram, R., Humphrey, V., Gerken, T., Feng, S., Digangi, J. P., and Frankenberg, C.: Cropland Carbon Uptake Delayed and Reduced by 2019 Midwest Floods, *AGU Advances*, 1, e2019AV000140, <https://doi.org/10.1029/2019av000140>, 2020.